Received: 14 March 2021 | Accepted: 6 July 2021

DOI: 10.1111/bpa.13010

Brain Pathology

RESEARCH ARTICLE

An integrative histopathological and epigenetic characterization of primary intracranial mesenchymal tumors, FET:CREB-fused broadening the spectrum of tumor entities in comparison with their soft tissue counterparts

Arnault Tauziède-Espariat[1,2] | Philipp Sievers[3,4] | Frédérique Larousserie[5] | Joseph Benzakoun[2,6] | Delphine Guillemot[7,8] | Gaëlle Pierron[7,8] | Mathilde Duchesne[9] | Emmanuelle Uro-Coste[10,11,12] | Alexandre Roux[2,13] | Alexandre Vasiljevic[14] | Tanguy Fenouil[14] | David Meyronet[14] | Karima Mokhtari[15] | Marc Polivka[16] | Audrey Rousseau[17] | Frédérique Bost-Bezeaud[18] | Samir Akoury[19] | Johan Pallud[2,13] | Chiara Benevello[13] | Lauren Hasty[1] | Albane Gareton[1] | Emmanuèle Lechapt[1] | Fabrice Chrétien[1] | Thomas Blauwblomme[20] | Kévin Beccaria[20] | Stéphanie Puget[20] | Felix Sahm[3,4,21] | Pascale Varlet[1,2] | the RENOCLIP-LOC

[1]Department of Neuropathology, GHU Paris-Psychiatrie et Neurosciences, Sainte-Anne Hospital, Paris, France

[2]Institut de Psychiatrie et Neurosciences de Paris (IPNP), UMR S1266, INSERM, IMA-BRAIN, Paris, France

[3]Department of Neuropathology, Institute of Pathology, University Hospital Heidelberg, Heidelberg, Germany

[4]Clinical Cooperation Unit Neuropathology, German Consortium for Translational Cancer Research (DKTK), German Cancer Research Center (DKFZ), Heidelberg, Germany

[5]Department of Pathology, Cochin Hospital, AP-HP Paris, Université de Paris, Paris, France

[6]Department of Radiology, GHU Paris-Psychiatrie et Neurosciences, Sainte-Anne Hospital, Paris, France

[7]Paris-Sciences-Lettres, Institut Curie Research Center, INSERM U830, Paris, France

[8]Laboratory of Somatic Genetics, Institut Curie Hospital, Paris, France

[9]Department of Pathology, Dupuytren University Hospital, Limoges, France

[10]Department of Pathology, Toulouse University Hospital, Toulouse, France

[11]Cancer Research Center of Toulouse (CRCT), INSERM U1037, Toulouse, France

[12]Toulouse III, Université Paul Sabatier, Toulouse, France

[13]Department of Neurosurgery, GHU Paris-Psychiatrie et Neurosciences, Sainte-Anne Hospital, Paris, France

[14]Department of Pathology and Neuropathology, GHE, Hospices civils de Lyon, France

[15]Department of Neuropathology, Pitié-Salpêtrière Hospital, AP-HP Paris, Paris, France

[16]Department of Pathology, Lariboisière Hospital, AP-HP Paris, Paris, France

[17]Department of Pathology, Angers Hospital, Angers, France

[18]Department of Pathology, Hospital of French Polynesia, Tahiti, France

[19]Department of Neurosurgery, Hospital of French Polynesia, Tahiti, France

[20]Department of Paediatric Neurosurgery, Necker Hospital, APHP, Université Paris Descartes, Sorbonne Paris Cité, Paris, France

[21]Hopp Children's Cancer Center Heidelberg (KiTZ, Heidelberg, Germany

Felix Sahm and Pascale Varlet are contributed equally to this work.

This is an open access article under the terms of the Creative Commons Attribution-NonCommercial-NoDerivs License, which permits use and distribution in any medium, provided the original work is properly cited, the use is non-commercial and no modifications or adaptations are made.
© 2021 The Authors. *Brain Pathology* published by John Wiley & Sons Ltd on behalf of International Society of Neuropathology

Correspondence
Arnault Tauziède-Espariat, Department of Neuropathology. GHU Paris-Psychiatrie et Neurosciences, Sainte-Anne Hospital, 1, rue Cabanis, Paris 75014, France.
Email: a.tauziede-espariat@ghu-paris.fr

Abstract

FET:CREB fusions have been described in a variety of tumors from various phenotypes. Recently, these fusion transcripts were reported in intracranial tumors, variably named intracranial mesenchymal myxoid tumors or angiomatoid fibrous histiocytomas. Controversy remains concerning the terminology for these tumors. Here, we report 11 cases of central nervous system mesenchymal tumors with proven FET:CREB fusion. Most DNA methylation profiles were not classifiable using the Heidelberg Brain Tumor or Sarcoma Classifier (v11b4/v12.2). However, by using unsupervised t-SNE and hierarchical clustering analyses, six of the cases constituted a distinct cluster. The remaining four tumors showed no obvious relation to any of the other referenced classes but were close to the clusters of extra-CNS angiomatoid fibrous histiocytomas (n = 1), clear cell sarcomas (n = 1), or solitary fibrous tumors (n = 2). Our findings confirm that intracranial FET:CREB-fused tumors do not represent a single molecular tumor entity, although most samples clustered close to each other, indicating the existence of a distinct epigenetic group that could potentially be partially masked by the low number of cases included. Further analyses are needed to characterize intracranial FET:CREB fused-defined tumors in more detail.

KEYWORDS
angiomatoid fibrous histiocytoma, Brain tumor, DNA methylation profile, EWSR1, myxoid

1 | INTRODUCTION

FET (encompassing both *EWSR1* and *FUS* genes) fusions with genes from the CREB (cAMP response element) family genes (*CREB1*, *CREM*, and *ATF1*) are involved in a wide variety of tumoral entities, and their correlations with tumor phenotypes have not been fully clarified. Among them, angiomatoid fibrous histiocytomas (AFH), clear cell sarcomas (CCS), gastrointestinal neuroectodermal tumors (GNET), and primary pulmonary myxoid sarcomas (PPMS) present clinical (location, age at diagnosis, prognosis), histopathological, and even molecular (frequency of gene fusion partner) differences. AFH are classically benign soft tissue tumors usually located in the extremities of children and young adults (1–4). Histopathologically, AFH are defined by a morphological triad: (1) blood-filled pseudoangiomatoid cystic spaces, (2) a lymphoplasmacytic peripheral cuff, and (3) a fibrous pseudocapsule. A myxoid variant has been described (2,5–12). The molecular hallmark of AFH is represented by a fusion of *EWSR1* with mostly the *CREB1* gene (83% of cases in five series), and occasionally with the *ATF1* gene (17% of cases in five series) (7,13–16). The *FUS:ATF1* gene was also described exceptionally (17) and only one recent case was reported having *EWSR1:CREM* fusion (18). CCS are malignant tumors found in the soft tissue, histopathologically characterized by nests of large clear cells and the expression of melanocytic markers (HMB45 and Melan-A) (19). More than 90% of CCS tumors harbor an *EWSR1:ATF1* fusion, whereas *CREB1* and *CREM* tumors have been, respectively, rare and only exceptionally described (19). The recent literature identified a novel intracranial histomolecular entity, variably referred to as the intracranial myxoid mesenchymal tumor (IMMT) or the intracranial AFH (44 reported cases to date) (16,20–41). In the CNS, because these tumors mostly lacked the characteristically histopathological triad of typical AFH of the soft tissue and because they often presented a myxoid stroma, the terminology "intracranial myxoid mesenchymal tumor" has been preferred by some authors (21,22,25,27,30,31,33,36,39–41). This controversial nosology will remain until further clarification as to whether this intracranial entity represents a new distinct histomolecular tumor type, or a myxoid variant of AFH. To explore this issue, we extensively studied proven FET:CREB intracranial tumors and screened our local and national French neuropathological network databases [n = 11, one of them was previously reported in (42)]. Our aim was to discover division or not into several (clinical, imaging, histopathological, and DNA methylation) subgroups or into one single group. We also compared their methylation profiles to sarcomas from extra-CNS sites.

2 | METHODS

2.1 | Sample collection

Tumor samples and retrospective clinical data from the 11 patients were provided by the consultation archive database (1982–2020) of the Sainte-Anne Hospital pathology department and by French expert centers from the RENOCLIP-LOC network. Case selection was based on tumors with *EWSR1* rearrangement by FISH analysis and/or with a FET:CREB fusion.

2.2 | Clinical and radiological data

Patient characteristics and clinical data retrieved from hospital records included: sex, age at presentation, and medical history. The central radiological review of preoperative magnetic resonance imagings (MRIs) was performed by a senior neuroradiologist (JB). The following features were evaluated: location (intra- or extra-axial, intraventricular, supra- or infra-tentorial), size, volume, signal in T1-weighted sequence, T2-weighted sequence, susceptibility imaging, diffusion and apparent coefficient diffusion map (ADC), contrast enhancement, contours, presence of cysts, necrosis, and dural tail, bone involvement, and perfusion parameters.

2.3 | Combined CNS and soft tissue experts' histopathological review

The central pathology review was performed conjointly by two neuropathologists (ATE and PV) and a pathologist expert in soft tissue tumors (FL). The analyses of tissue were performed in accordance with local ethics regulations.

2.4 | Immunohistochemistry

A representative paraffin block was selected for each case. Unstained 3-μm-thick slides of formalin-fixed, paraffin-embedded tissues were obtained and submitted for immunostaining. The following primary antibodies were used: Glial Fibrillary Acidic Protein (GFAP) (1:200, clone 6F2, Dako, Glostrup, Denmark), SSTR2a (1:200, clone UMB1, Abcam, Cambridge, UK), epithelial membrane antigen (1:200, clone GM008, Dako, Glostrup, Denmark), CKAE1AE3 (1:800, clone AE1AE3, Dako, Glostrup, Denmark), CD99 (1:10, clone 12E7, Dako, Glostrup, Denmark), S100 (1:200, clone 6F2, Dako, Glostrup, Denmark), SOX10 (1:200, clone IHC010, Diagomics, Blagnac, France), CD68 (1:400, clone KP1, Dako, Glostrup, Denmark), CD56 (pre-diluted, clone 123C3, Dako, Glostrup, Denmark), synaptophysin (1:150, clone DAK-SYNAP, Dako, Glostrup, Denmark), alpha-smooth muscle actin (1:6000, clone S100, Dako, Glostrup, Denmark), HMB45 (1:50, clone HMB45, Dako, Glostrup, Denmark), Melan-A (prediluted, clone A103, Roche Diagnostics, Burgess Hill, UK), desmin (1:200, clone D33, Dako, Glostrup, Denmark), MUC4 (1:200, clone 8G7, Santa Cruz Biotechnology, Santa Cruz, CA), ALK (1:50, clone 5A4, Leica Biosystems, Newcastle Upon Tyne, UK), CD34 (1:40, clone Qbend10, Dako, Glostrup, Denmark), INI1 (BAF47) (1:50, clone 25/BAF 47, BD Biosciences, Franklin Lakes, USA), and Ki-67 (1:200, clone MIB-1, Dako, Glostrup, Denmark). External positive and negative controls were used for all antibodies.

2.5 | DNA methylation array processing and copy number profiling

Genomic DNA was extracted from fresh-frozen or formalin-fixed and paraffin-embedded (FFPE) tissue samples. DNA methylation profiling of all samples was performed using the Infinium MethylationEPIC (850k) BeadChip (Illumina, San Diego, CA, USA) or Infinium HumanMethylation450 (450k) BeadChip array (Illumina) as previously described [2]. All computational analyses were performed in R version 3.3.1 (R Development Core Team, 2016; https://www.R-project.org). Copy-number variation analyses from 450k and EPIC methylation array data were performed using the conumee Bioconductor package version 1.12.0. Raw signal intensities were obtained from IDAT-files using the minfi Bioconductor package version 1.21.4 [1]. Illumina EPIC samples and 450k samples were merged to a combined data set by selecting the intersection of probes present on both arrays (combineArrays function, minfi). Each sample was individually normalized by performing a background correction (shifting of the 5% percentile of negative control probe intensities to 0) and a dye-bias correction (scaling of the mean of normalization control probe intensities to 10,000) for both color channels. Subsequently, a correction for the type of material tissue (FFPE/frozen) and array type (450k/EPIC) was performed by fitting univariable, linear models to the log2-transformed intensity values (removeBatchEffect function, limma package version 3.30.11). The methylated and unmethylated signals were corrected individually. Beta-values were calculated from the retransformed intensities using an offset of 100 (as recommended by Illumina). All samples were checked for duplicates by the pairwise correlation of the genotyping probes on the 450k/850k array. To perform unsupervised non-linear dimension reduction, the remaining probes after standard filtering [2] were used to calculate the 1-variance weighted Pearson correlation between samples. The resulting distance matrix was used as input for t-SNE analysis (t-distributed stochastic neighbor embedding; Rtsne package version 0.13). The following non-default parameters were applied: theta = 0, pca = F, max_iter = 20,000 perplexity = 10.

2.6 | RNA sequencing and clustering

Complete RNA samples were extracted from snap-frozen tumors using the TRIzol/chloroform method (Chomczynski and Sacchi, 1987) (Thermo Fisher Scientific, Carlsbad, CA, USA) and were qualified with fragment analysis by TapeStation 4200 (Agilent Technologies, Carlsbad, CA, USA). Libraries were prepared using TruSeq mRNA-stranded library kits (Illumina, Inc., San Diego, CA, USA). One microgram of total RNA per sample was purified, reverse transcribed, fragmented, indexed, and amplified to make the RNA library. Libraries were sequenced over 2 × 150 pb with a 500 High Output v2 on NextSeq500 (Illumina, Inc., San Diego, CA, USA). Expression data were generated using Star Aligner (V2.5.3a) and count matrices using FeatureCount (V1.6.0). The count matrices were normalized in FPKM. Data were used for a clustering analysis (Ward method and correlation Spearman or Pearson with or without Internal Quantil Range) and also used for boxplot generation. For principal component analyses, the gene expression matrix (TPM) was normalized and genes with at least 0.5 TPM in 20% of all samples were kept for further analysis. Analyses were performed in the R software. Clustering by principal component analysis was performed with the prcomp function. A fusion analysis was performed from FastQ with two approaches. (1) a targeted analysis using dedicated reference fusion sequences implemented with known fusions of each tumor type. (2) an exploration analysis using five fusion finder tools (TopHat fusion v2.0.6, Defuse V0.6.0, StarFusion V2.5.3, Fusion Catcher v1.00, and FusionMap). The fusion interpretation combines both results of the targeted fusion and those of the exploration analysis. To perform cluster analysis, we used the UMAP (Uniform Manifold Approximation and Projection) technique which is a practical scalable algorithm, complementary of t-SNE, based on the expression data (using STAR v2.7 gencode v19 and Seurat package on R). In our study, the RNA values of the four cases were compared with a dataset of tumors with *EWSR1* fusion with a gene of the *CREB* family (six AFH of the soft tissue; nine clear cell sarcomas), meningiomas (n = 25), and fibrous solitary tumors (SFT) (n = 26) of the meninges (n = 11) or other sites (n = 15). Gene expression data were extracted using the Kallisto v0.42.5 tool with GENECODE to release 23 genome annotations based on the GRCh38 genome reference. Clustering was performed with the R package Cluster v2.0.3 ConsensusClusterPlus v1.46.

2.7 | Ultrastructural analyses

A representative section was first selected for each case on formalin-fixed, paraffin-embedded tissues stained with Hemalun Phloxin Saffron. Then, tissues were deparaffinized and fixed for1 h in glutaraldehyde. After dehydration processing, tissues were embedded in Epon. Semi-thin sections (1-µm-thick slides) were stained with toluidine blue. Ultrathin sections (90 nm) were stained with lead citrate and uranyl acetate, then observed under an electronic microscope (JEOL JEM 1400 Flash). Analysis was performed at the Limoges University Hospital in the Pathology Department by one neuropathologist (MD).

3 | RESULTS

3.1 | Clinical and radiological characteristics

The clinical data of the patients are detailed in Table 1. The median age of presentation in our cohort was 23 years (ranging from 8 to 73). Four patients (36%) were children. The female-to-male ratio was 0.6 (four females and seven males). Three patients (Cases #3, 7, and 9) had a clinical history of lymphomas (of different histopathologies) and two other have, respectively, a previous history of breast cancer (Case #2) and allograft for mucopolysaccharidosis (Case #8). All tumors were extra-parenchymal, mostly supratentorial (10/11 cases), and two cases were intraventricular. Data from treatment and follow-up were available for all patients (for details see Table 1). A gross total resection was achieved in 9/11 patients with no residual disease checked on the postoperative central neuroradiological review. Two patients underwent focal radiation therapy and one patient received adjuvant chemotherapy. Most cases (8/11) were free of disease at 2 to 53 months (mean, 25 months; median, 27 months) including three cases with >3-year survival after resection. Interestingly, those cases were treated only by gross total resection. Two patients presented a local recurrence after an incomplete resection and another presented a local recurrence more than 10 years after the initial resection, but these three patients are currently alive and well. There was no evidence of metastatic disease in any patient. Preoperative imaging was available in 9/11 patients. Radiologically, five lesions (56%) were purely extra-axial, 2 (22%) were extra-axial with cortical involvement (Cases 5 and 6), and two (22%) were intraventricular (Cases 8 and 9). The mean lesion diameter was 37 mm (±8 mm) and mean volume was estimated at 75 ml (±69). In seven patients, where an unenhanced T1-weighted sequence was available, all lesions were hypointense. In eight patients, where the T2-weighted sequence was available, three tumors (37%) presented a high or very high T2 intensity with hypointense septa, and five (63%) were heterogeneous and hypointense. In four patients where susceptibility imaging was available, three (75%) presented with hypointense foci, often peripheral, that could represent hemorrhagic changes. In six patients where diffusion sequence was available (Cases #1, 3, 6, 7, 9, and 11), all lesions were hypointense, with increased ADC (mean value: $1.590 \pm 588 \times 10^{-3}$ $mm^2.s^{-1}$) and four

TABLE 1 Summary of clinical characteristics of cases of our series

Case	Age (y), sex	Medical history	Site of the tumor	Treatments	Recurrence, PFS (m)	Status at the end of follow-up, OS (m)
1	20, M	0	Extra-axial Right parieto-occipital	GTR, RT, CT	Local, 119	Alive, 158
2	59, F	Breast cancer	Extra-axial Right para-sagittal	PR	Local, 10	Alive, 17
3	15, F	Mediastinal lymphoblastic lymphoma	Extra-axial Left para-sagittal	GTR	0	Alive, 36
4	73, M	0	Sellar	GTR	0	Alive, 36
5	50, F	0	Extra-axial Right cerebellar	GTR	0	Alive, 10
6	41, M	0	Extra-axial Falx cerebri	PR, RT	Local, 49	Alive, 80
7	8, M	Orbit Burkitt lymphoma	Extra-axial Falx cerebri	GTR	0	Alive, 23
8	16, M	Mucopolysaccharidosis	Intra-ventricular	GTR	0	Alive, 53
9	23, M	Hodgkin lymphoma	Intra-ventricular	GTR	0	Alive, 6
10	38, F	0	Extra-axial Left parieto-occcipital	GTR	0	Alive, 2
11	16, M	0	Extra-axial Left parietal	GTR	0	Alive, 31

Abbreviations: CT, chemotherapy; F, female; GTR, gross total resection; M, male; m, months; PR, partial resection; RT, radiation therapy; Y, years old.

(67%) had a peripherally decreased ADC rim. All lesions presented an enhanced tissular portion and lobulated contours. Cystic components were present in 5/9 lesions (56%, Cases #5, 6, 7, 8, and 11). Dural tail was present in only two out of seven (29%, Cases #1 and 7) lesions with an extra-axial component. No bone involvement was found. In three patients explored with perfusion imaging (Cases #1, 3, and 7), all displayed hyperperfusion (relative cerebral blood volume ≥10).

3.2 | Histopathological and immunohistochemical characterization

All tumors were multinodular at low-power magnification and were well-circumscribed by a fibrous pseudocapsule (in 4/4 of the evaluable samples). Lymphoplasmacytic infiltrates were present in 6/11 cases, constituting a peritumoral cuff in only three cases. Follicles with germinal centers were encountered in 1/11 cases. No multinucleate giant cells were present. Only one case (#10) presented blood-filled pseudoangiomatoid spaces. A prominent myxoid stroma, representing more than 60% of the tumor surface in the available histological sections, was present in 8/11 cases. The cellular density was variable, low in nine tumors, and high in three cases (#1, 5, and 11). In 10/11 cases, tumor cells were histiocytoid or spindle-shaped with mildly atypical oval or polygonal vesicular nuclei, inconspicuous nucleoli, and eosinophilic cytoplasm with ill-defined borders. In one case (#1), tumor cells were epithelioid with clear cell cytoplasm. Intranuclear cytoplasmic inclusions were observed in all cases. In a subset of cases, hemosiderin deposition (6/11 cases) and cystic degeneration (3/11) were present. The vascularization was well-developed with thin-walled branching vessels (11/11 cases) or a pseudoangiomatous appearance (9/11 cases). No staghorn vessels were observed. Calcifications (but no psammoma bodies), osseous metaplasia, and a pseudochondroid matrix were evidenced in one case, respectively. Amianthoid fibers were observed in 6/11 cases. Necrosis was absent in all cases and mitoses were scant (0 to 8 per 10 high-power fields, so 3.2 mm^2, with a mean of three mitoses), except in the recurrence of Case #1 which presenting necrosis and a high mitotic index (54 per 10 high-power fields). Ki-67 labeling activity was very low (1%–8%) in all primary tumors. By immunohistochemistry, all tumors expressed CD68 and EMA. Desmin was variably stained (absent in Case #1, focal in Cases #4 and 8, as part of tumor cells in cases #2, 3, 5, 6, 7, 9, and 11, and diffuse in Case #10, respectively). CD99 (6/11), S100-protein (9/11), and MUC4 (3/11 cases, with only focal staining) and CKAE1AE3 (1/11) were expressed in a subset of tumors. Focal expression of SSTR2A was evidenced in 3/11 cases. Staining for smooth muscle-actin, CD34, GFAP, CD56, synaptophysin, SOX10, HMB45, Melan-A, and ALK was constantly negative. INI1 expression was retained in all cases.

3.3 | DNA methylation profiling

DNA-methylation profiles were obtained from 10 tumor samples with sufficient DNA quality. Using DNA methylation-based classification and the Heidelberg Brain Tumor and Sarcoma Classifiers (version 11b4/12.2), none of the tumors were classifiable (calibrated scores for DNA methylation class <0.9). Next, a t-Distributed Stochastic Neighbor Embedding (t-SNE) analysis was performed in comparison with the genome-wide DNA methylation profiles of the sarcoma reference cohort (43) as well as a more focused analysis with selected reference groups. While six of the cases grouped together close to the clusters of meningioma and solitary fibrous tumor, the remaining four cases showed no obvious relation to any of the other reference classes but were close to the clusters of extra-CNS angiomatoid fibrous histiocytomas (n = 1), clear cell sarcomas (n = 1), or solitary fibrous tumors (n = 2) (Figure 1).

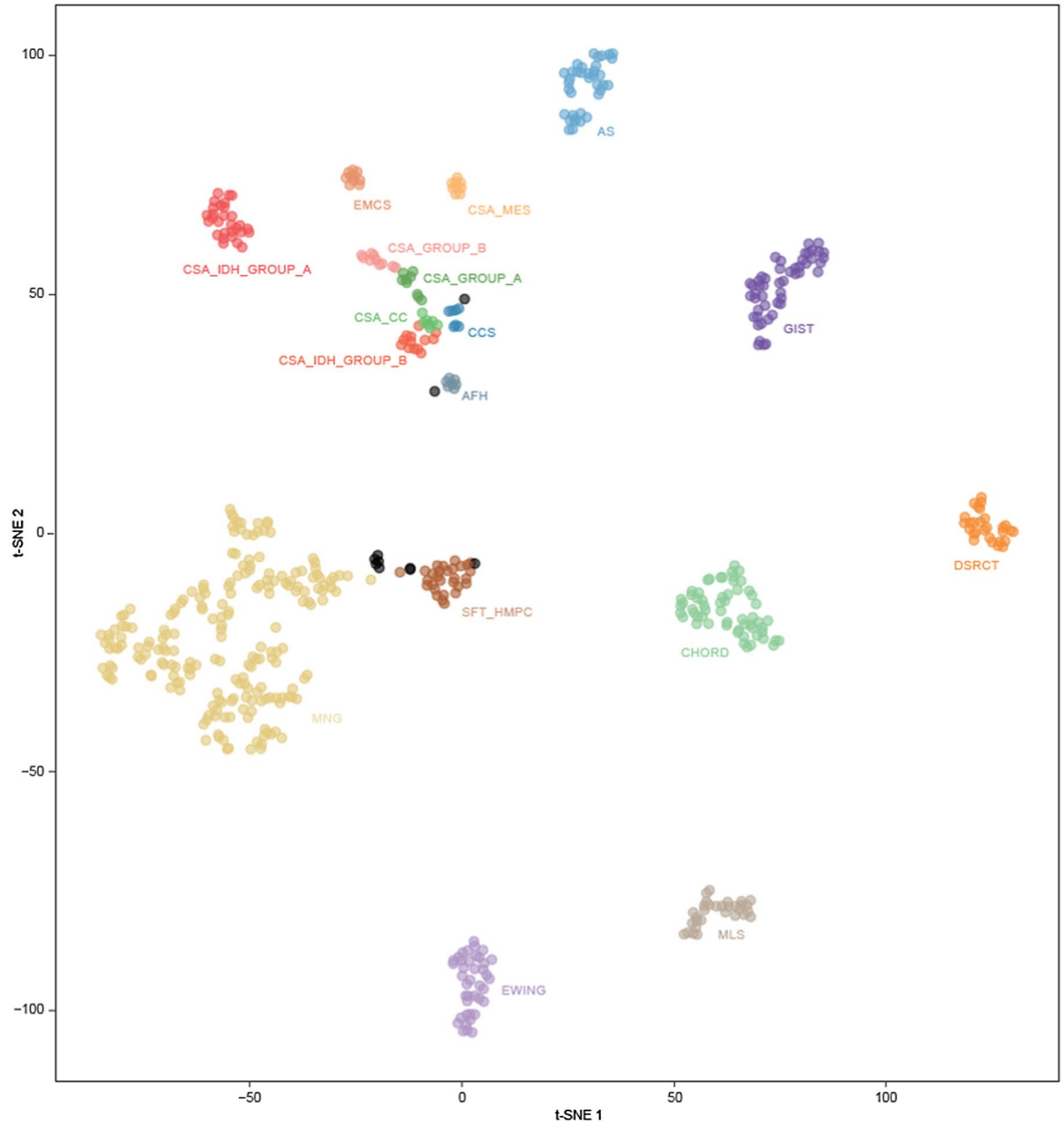

FIGURE 1 t-distributed stochastic neighbor embedding (t-SNE) analysis of DNA methylation profiles of the 10 investigated tumors alongside selected reference samples. Reference DNA methylation classes: angiomatoid fibrous histiocytoma (AFH), angiosarcoma (AS), clear cell sarcoma of soft parts (CCS), chordoma (CHORD), clear cell chondrosarcoma (CSA_CC), chondrosarcoma group A (CSA _Group_A), chondrosarcoma group B (CSA_Group_B), chondrosarcoma IDH mutant group A (CSA_IDH_Group_A), chondrosarcoma IDH mutant group B (CSA_IDH_Group_B), chondrosarcoma mesenchymal (CSA_MES), desmoplastic small round cell tumor (DSRCT), extraskeletal myxoid chondrosarcoma (EMCS), ewing sarcoma (EWING), gastrointestinal stromal tumor (GIST), myxoid liposarcoma (MLS), meningioma (MNG), solitary fibrous tumor/hemangiopericytoma (SFT_HMPC)

3.4 | RNA sequencing and clustering results

Transcript fusions are summarized in Table S1. Unsupervised cluster analysis showed that both CNS tumors with an *EWSR1* fusion formed a common cluster, independent of meningiomas and SFT, but in vicinity to their extra-CNS counterparts, particularly the soft tissue AFH (Figure S1).

3.5 | Ultrastructural results

Ultrastructural analyses were available for six cases (Cases #1, 2, 3, 5, 7, and 8). All tumors showed intercellular junction-type desmosomes, *zonula occludens*, *zonula adherens*, and extra-cellular collagen (Figure S2). To note, no electron-dense granules, no melanosomes, no clear vesicles, and no dense-core granules were identified in any case. There were intranuclear cytoplasmic inclusions.

3.6 | Integrative histomolecular diagnosis

Case #10 classified close to AFH of the soft tissue by t-SNE analysis was the unique case of our series to present histopathology of classical AFH (Figure 2). The morphological triad (including cystic pseudoangiomatoid spaces) was clearly visible with a thick fibrous capsule and the most prominent lymphocytic peripheral cuff of tumors of our series. Moreover, there was no prominent myxoid stroma. The tumor harbored an *EWSR1:ATF1* fusion.

Case #1 was different radiologically (no cystic component) and morphologically from the other cases of our series, presenting necrosis, and an elevated mitotic index. It presented an epithelioid pattern composed of nests of cohesive clear cells (Figure 3). Despite the absence of immunoexpression of melanocytic markers and the presence of an *EWSR1:CREM* fusion, this tumor clustered in close vicinity with CCS by t-SNE analysis.

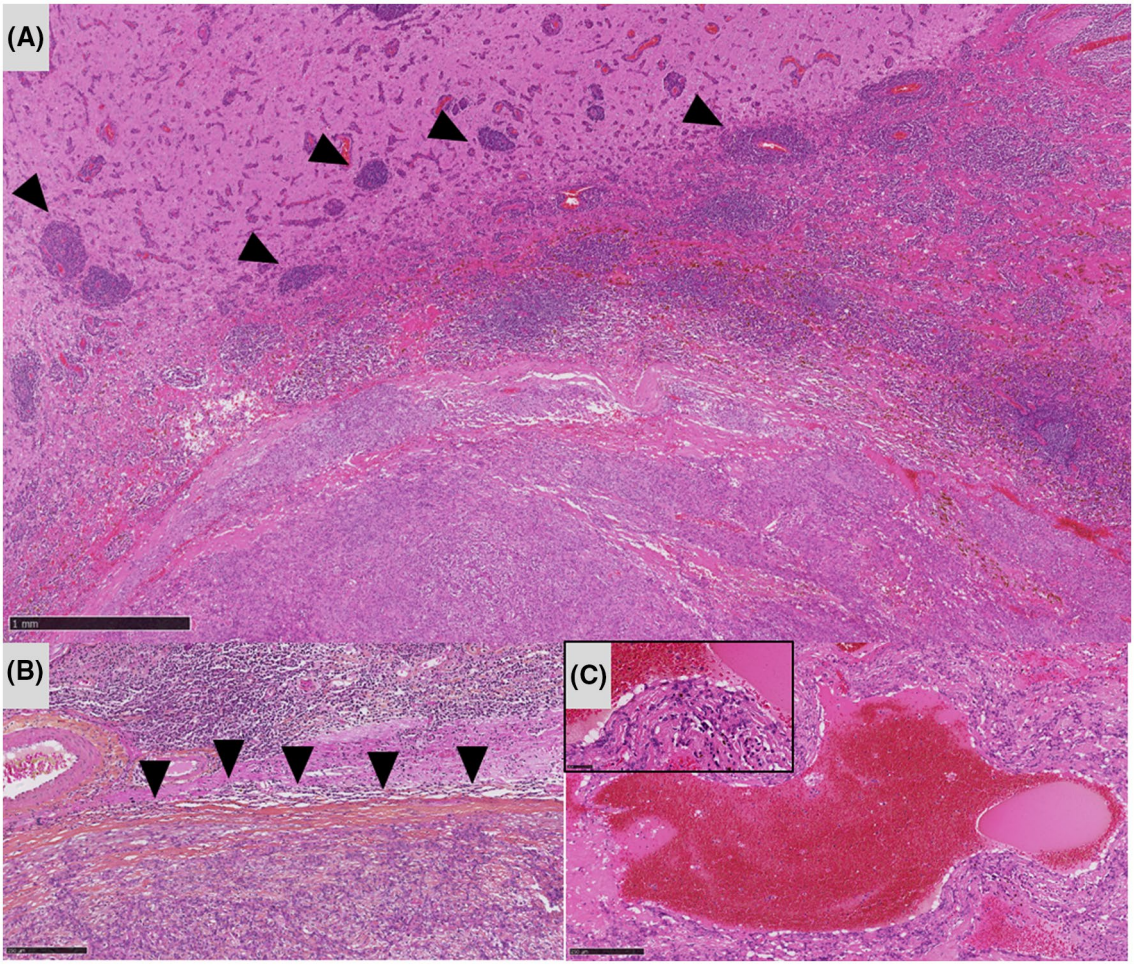

FIGURE 2 Histopathological features of Case #10. (A) Prominent peritumoral lymphoplasmacytic infiltrates (arrowheads) around the fibrous pseudcapsule (HPS, magnification x40). (B) Well-circumscribed tumor delineated by a fibrous pseudocapsule (arrowheads) (HPS, magnification x100). (C) Cystic pseudoangiomatoid space lined by tumor cells (HPS, magnification x90, and insert magnification x400). Black scale bars represent 1 mm (A), 500 µm (B), and 250 µm (C). HPS, hematoxylin phloxin saffron

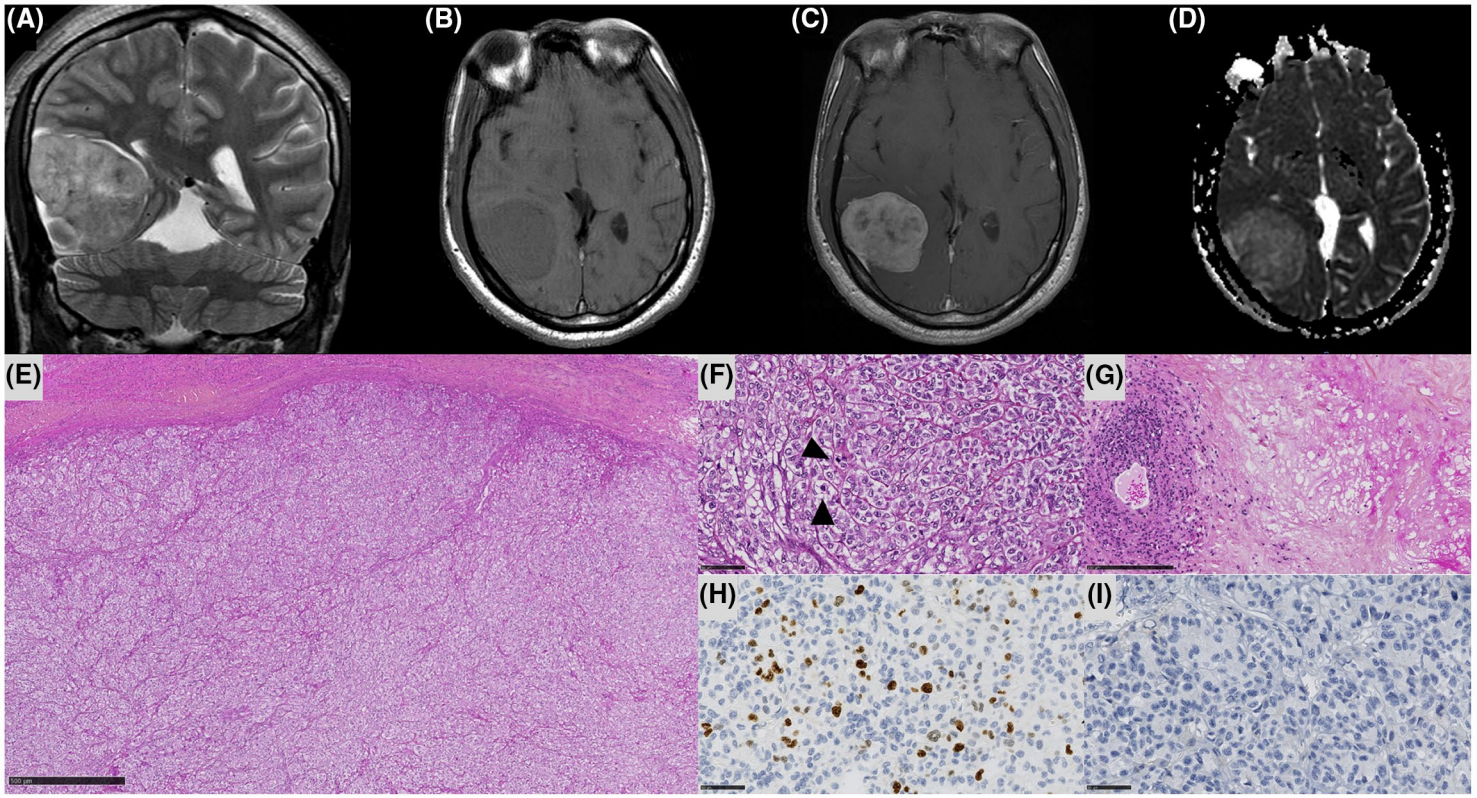

FIGURE 3 Radiological and histopathological features of Case #1. (A) Extra-axial lesion without peritumoral edema, with low signal on axial T2-weighted sequence (B) and T1-weighted sequence. After contract injection (C), the lesion presented heterogeneous and intense enhancement, and displayed a dural tail. ADC map (D) displayed a central increase of diffusion coefficient. (E) Well-circumscribed epithelioid tumor (HPS, magnification x60), composed of cohesive clear cells with numerous mitoses (arrowheads) (F, HPS, magnification x400) and necrosis (G, HPS, magnification x150). (H) Increased MIB-1 labeling index (magnification x400). (I) Absence of the expression of desmin by tumor cells. Black scale bars represent 500 μm (E), 50 μm (F, H, and I), and 250 μm (G). HPS, hematoxylin phloxin saffron

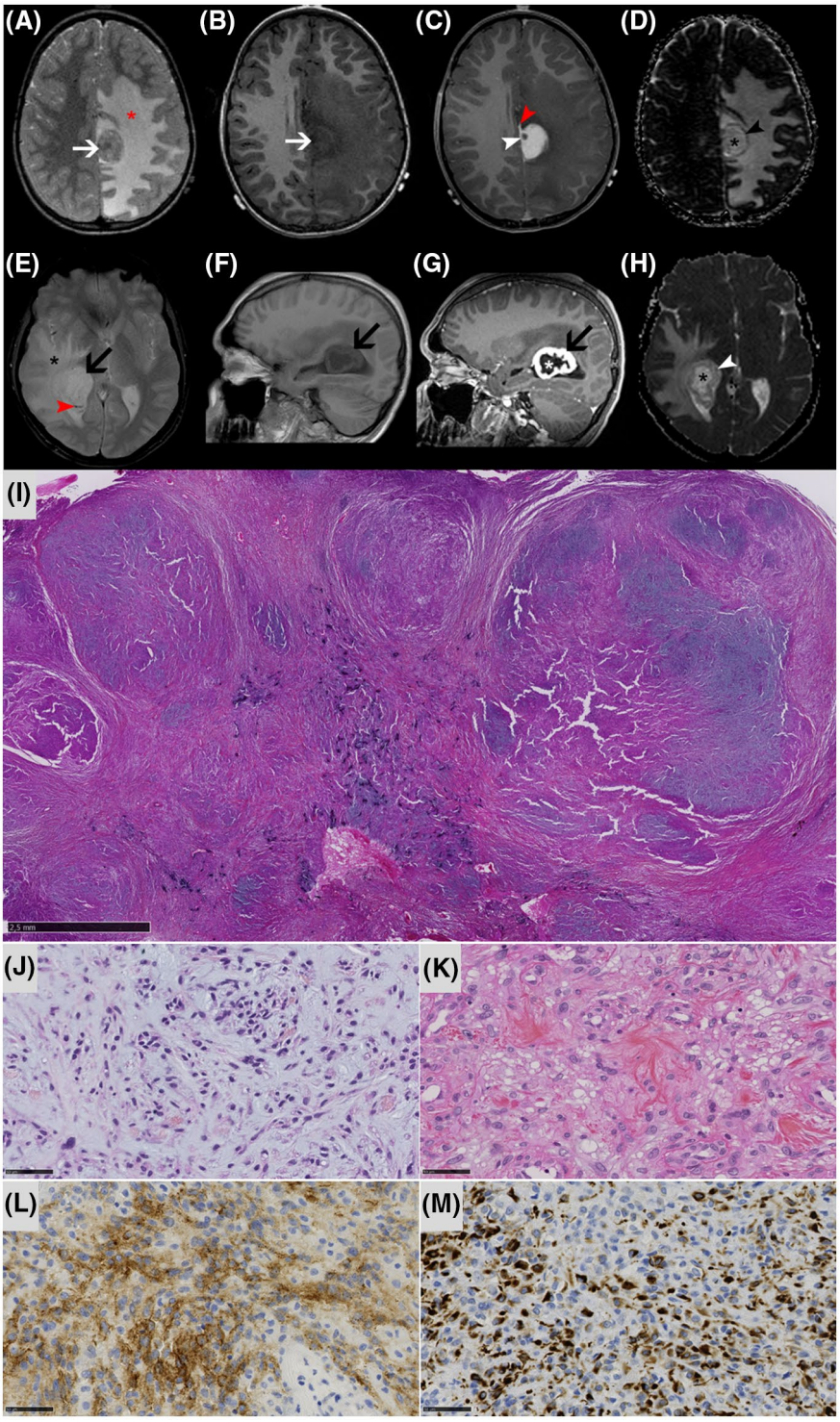

FIGURE 4 Radiological and histopathological features of Cases #7 and 9. Case 7 (upper row, A–D) displayed an extra-axial interhemispheric lesion with low signal on axial T2-weighted sequence (arrow in A) and T1-weighted sequence (arrow in B) surrounded with large peritumoral edema (red asterisk in A). After contract injection (C), the lesion presented homogenous and intense enhancement, and displayed a peripheral cyst (white arrowhead) and a dural tail (red arrowhead). ADC map (D) displayed a central increase of diffusion coefficient (asterisk) and a peripheral decrease (arrowhead). Case 9 (lower row, E–H) presented a right intraventricular lesion. This lesion was highly hyperintense in axial T2* sequence (E) with peripheral susceptibility hypointensities (red arrowheads) and large peripheral edema (asterisk). On sagittal T1-weighted sequence before (F) and after (G) contrast injection, the lesion presented a peripheral enhanced tissular portion (black arrow) and a central unenhanced portion (white asterisk in G). ADC map (H) displayed an increase of diffusion coefficient inside the necrotic component (asterisk) and intermediate diffusion coefficient in the tissular component (arrowhead in H). (I) Well-circumscribed and multilobulated tumor (HPS, magnification x10). (J) Myxoid stroma in the tumor (HPS, magnification x400). (K) Amianthoid fibers (HPS, magnification x400). (L) Expression of EMA (magnification x400). (M) Expression of desmin (magnification x400). Black scale bars represent 2,5 mm (I), 50 µm (J–M). HPS, hematoxylin phloxin saffron

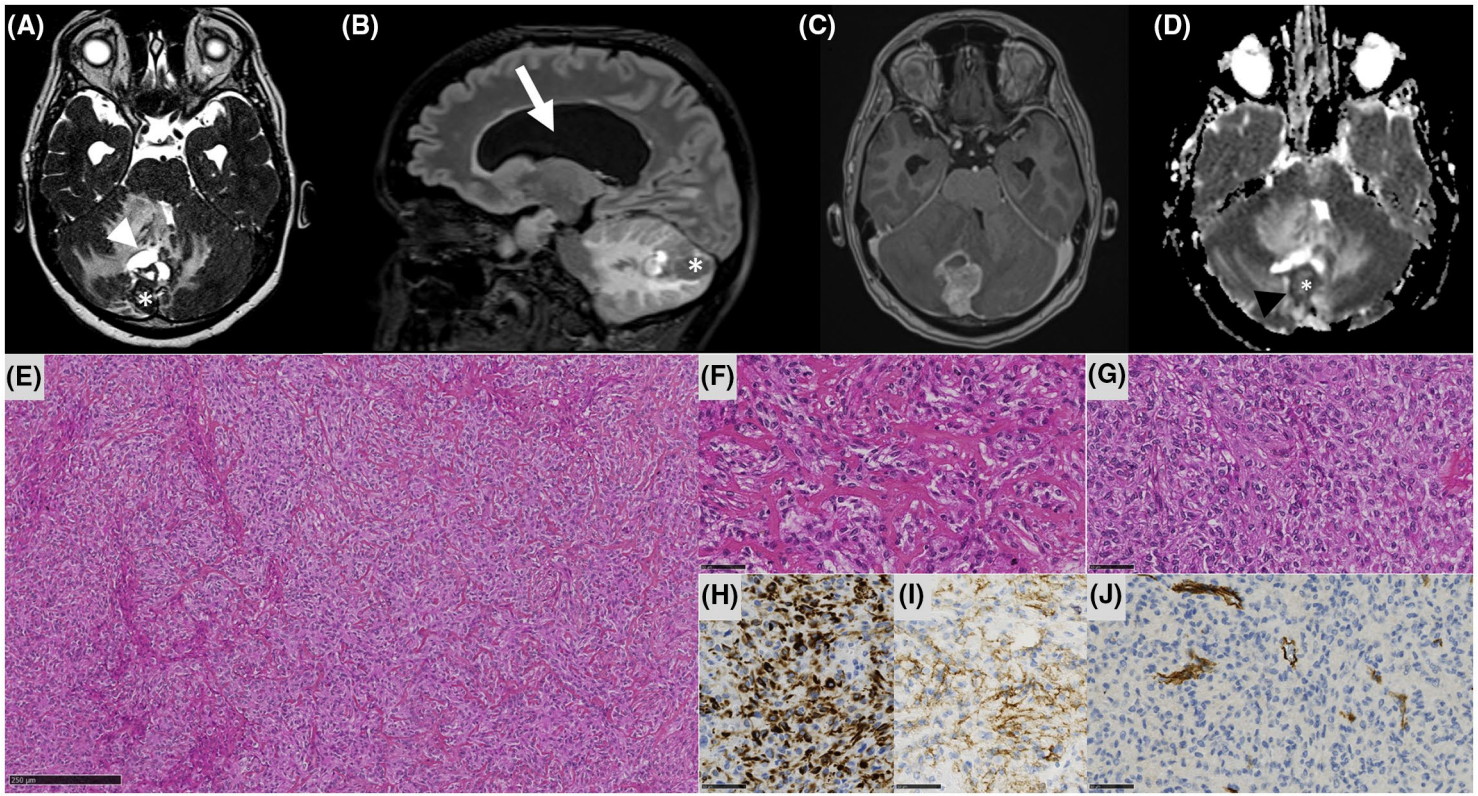

FIGURE 5 Radiological and histopathological features of Case #5. (A) Posterior fossa lesion with cystic (arrowhead) and solid (asterisk) components, associated with large peritumoral edema with mass effect on the fourth ventricle (arrow) on axial T2-weighted sequence. (B) On sagittal T2 Fluid-attenuated Inversion recovery (FLAIR) weighted sequence, solid component is hypointense (asterisk) and associated hydrocephalus is visible (arrow). (C) After contract injection, the lesion presented lobulated contours, with heterogeneous and intense enhancement. (D) ADC map displayed a peripheral decrease (arrowhead) and a central increase (asterisk) of diffusion coefficient. (E) Highly cellular tumor (HPS, magnification x100), composed of thick collagen fibers (F, HPS, magnification x400) and histiocytoid cells (G, HPS, magnification x400). (H) Expression of desmin (magnification x400). (I) Expression of EMA (magnification x400). (J) Absence of expression of SSTR2A by tumor cells. Black scale bars represent 250 µm (E), 50 µm (F–J). HPS, hematoxylin phloxin saffron

Cases #2, 3, 6, 7, 8, and 9 clustered together between meningiomas and SFT by t-SNE analysis. Radiologically, they all were lobulated, well-delimited with a cystic component in most cases. Histopathologically, all cases presented nodules and an alternate of myxoid prominent stroma containing some cord-like cells and more cellular nodules with a variable fibrous collagenous stroma and frequent amianthoid fibers (Figure 4). All cases presented intranuclear cytoplasmic inclusions but no psammoma bodies or whorls-like structures were observed and they did not express diffusely SSTR2A. They shared the same locations as we can encounter in meningiomas, such as the falx cerebri and ventricles. Moreover, four cases with the available ultrastructural analysis presented junction-type desmosomes, *zonula occludens*, *zonula adherens*. Interestingly, four of these six patients (66%) had a previous history of chronic immunodepression (particularly lymphomas in Cases #3, 7, and 9).

The two last tumors (Cases #5 and 11) presented a higher cellular density composed of sheets of histiocytoid cells without atypia or mitoses (Figure 5). They did not present cystic pseudoangiectatic spaces and were well-circumscribed from the parenchyma, delineated by a thin fibrous capsule. The inflammatory peripheral cuff was made of scarce foci of lymphocytes. Myxoid modifications were present in one of the two cases but were not prominent. Collagen fibers were prominent in some areas of the tumors organized in thick bundles and with amianthoid fibers (Figure 5). By immunohistochemistry, they express EMA and desmin but did not stain with STAT6 and SSTR2A (Figure 5). By DNA-methylation analysis, the t-SNE showed that they were in close vicinity with SFT. They harbored an *EWSR1:CREM* and an *EWSR1:ATF1* fusions.

4 | DISCUSSION

FET:CREB fusions are not an entity-specific molecular alteration. They can be found ubiquitously in a large variety of tumors having different phenotypes, such as CCS, clear cell sarcoma-like tumors of the gastrointestinal tract, AFH, and PPMS (14,18), among others. In the recent literature, a novel CNS tumoral entity has been described, characterized by FET:CREB fusions. The wide morphological and molecular overlap of these FET:CREB-fused CNS tumors with soft tissue AFH raises the question as to whether these tumors represent a spectrum of the same disorder or not. Here we studied a series of CNS tumors with FET:CREB fusion, and performed a comprehensive study including, for the first time, a DNA-methylation approach. Based on epigenetic profiling, our tumor series did not clearly form its own cluster different from all other established groups. However, we showed that the main subgroup of tumors (6/11 cases) did in fact cluster together, and were not classified as mesenchymal tumors in the sarcoma classifier but between meningiomas and SFT. Because DNA methylation profiles are thought to represent a combination of both somatically acquired DNA methylation changes and a signature reflecting the cell of origin (44), it is, therefore, reasonable to assume that tumors from the CNS represent a distinct entity from soft tissue AFH. Moreover, our cases presented ultrastructural (presence of junction-type desmosomes, *zonula occludens*, *zonula adherens*) and histopathological (absence of complete diagnostic triad) differences from AFH of the soft tissue (45–48). These tumors shared with meningiomas some histopathological (intranuclear cytoplasmic inclusions described in our cases and whorls described in reported cases) (38,49), radiological (tumor locations), and ultrastructural (junctions encountered in arachnoidal cells from the leptomeninges) characteristics. Furthermore, their epigenetic proximity with meningiomas can suggest a leptomeningeal cell origin for this new tumoral entity. However, our results seem to evidence that FET:CREB-fused intracranial tumors do not represent a new variant of meningioma. Radiologically, the presence of cystic areas was a more frequent feature in our series than in meningiomas (50). Most of the FET:CREB-fused intracranial tumors displayed a low diffusion signal and high ADC (mean ADC values of $1.590 \pm 588 \times 10^{-3}$ $mm^2.s^{-1}$ in our series compared to 0.96 and 0.80×10^{-3} $mm^2.s^{-1}$ for grade I or grade II/III meningiomas, respectively, in a previous series) (51), which may be a marker for low cellularity and a myxoid component (52,53). Histopathologically, meningiomas may present myxoid modifications (54,55), but lack the characteristic fibrous pseudocapsule and peritumoral lymphoplasmacytic cuff, as well as desmin expression by immunohistochemistry encountered in FET:CREB-fused intracranial tumors. Moreover, our series showed that in contrast to meningiomas, mesenchymal tumors of the CNS with FET:CREB fusion did not express diffusely SSTR2a, which is a diagnostic biomarker of meningioma (56). Accordingly to all these results, we suggest the terminology of "primary intracranial mesenchymal tumor, FET:CREB-fused" to designate these tumors. Histopathologically, specific features of those tumors included the constant EMA and desmin immunoexpressions and the frequent presence of amianthoid fibers.

Although most cases grouped together and the existence of a distinct methylation class could potentially be masked by the low number of cases included, the remaining tumor samples did segregate into different groups. First, one of our cases shared clinical (young age), radiological (presence of a cystic component) (57), histopathological (presence of the triad), and molecular (*EWSR1:ATF1* fusion, the preferential fusion transcripts in AFH of the soft tissue (2–5,7,8,12,13,15–18,58–64)) features with AFH of the soft tissue but no other tumor location was found. Further samples with DNA-methylation analyses are needed to confirm that true primary AFH exist in the CNS. Besides, one of our cases

presented histopathological similarities (clear cells, epithelioid pattern, without myxoid stroma associated with signs of malignancy, such as necrosis and elevated mitotic and MIB-1 labeling indexes) with CCS. However, because of the absence of the expression of melanocytic markers and the absence of electron-dense granules and melanosomes by ultrastructural analyses (65), the terminology of CCS cannot be retained. Another differential diagnosis could be a metastasis of a malignant gastrointestinal neuroectodermal tumor (which was never described to date in the CNS) but no neoplasm of the digestive tract was known in our patient, and our case did not express SOX10 and neuroendocrine markers which are frequently stained in this entity (66,67). Interestingly, our case was the only one to recur after total resection in our series. Despite these advances in the deciphering of FET:CREB-fused CNS tumors, our study showed that the two last cases did not cluster with the three previous subgroups and further cases have to be added to clearly delineate their origins.

To conclude, our study, based on DNA methylation profiling, has uncovered heterogeneity within what has previously been considered a single tumoral entity and clearly distinguished intracranial tumors from their soft tissue counterparts. However, our study evidenced that a subset of those tumors seems to delineate a new methylation class, that we suggest to designate as "primary intracranial mesenchymal tumors, FET:CREB-fused." Further studies are needed to characterize in detail this rare type of tumor and to validate the epigenetic findings that suggest a possible new cluster of tumors. In particular, correlations with the ultrastructural findings will be of interest because they show similarities between all cases, even those outside of the putative new cluster.

ACKNOWLEDGMENTS

We would like to thank the laboratory technicians at the GHU Paris Neurosciences, Hospital Sainte-Anne, for their assistance.

CONFLICTS OF INTEREST

The authors declare that they have no conflict of interest directly related to the topic of this article.

AUTHOR CONTRIBUTIONS

Arnault Tauziède-Espariat, Frédérique Larousserie, Mathilde Duchesne, Emmanuelle Uro-Coste, Alexandre Vasiljevic, Tanguy Fenouil, David Meyronet, Karima Mokhtari, Marc Polivka, Audrey Rousseau, Frédérique Bost-Bezeaud, Albane Gareton, Emmanuèle Lechapt, Fabrice Chrétien, and Pascale Varlet conducted the histopathological examinations; Philipp Sievers, Delphine Guillemot, Gaëlle Pierron, and Felix Sahm conducted the molecular studies; Arnault Tauziède-Espariat, Lauren Hasty, and Pascale Varlet drafted the manuscript; Joseph Benzakoun reviewed all imaging data; Audrey Rousseau, Samir Akoury, Johan Pallud, Chiara Benevello, Thomas Blauwblomme, Kévin Beccaria, and Stéphanie Puget recruited patients, provided samples, and clinical information. All authors reviewed the manuscript.

DATA AVAILABILITY STATEMENT

The data that support the findings of this study are available from the corresponding author upon reasonable request.

ORCID

Emmanuelle Uro-Coste https://orcid.org/0000-0001-7300-5724
Albane Gareton https://orcid.org/0000-0002-3650-8581

REFERENCES

1. Abrahao-Machado LF, Bacchi LM, Fernandes IL, Costa FD, Bacchi CE. MUC4 expression in angiomatoid fibrous histiocytoma. Appl Immunohistochem Mol Morphol. 2020;28(8):641–5.
2. Chen G, Folpe AL, Colby TV, Sittampalam K, Patey M, Chen M-G, et al. Angiomatoid fibrous histiocytoma: unusual sites and unusual morphology. Mod Pathol. 2011;24(12):1560–70.
3. Khan IS, Kuick CH, Jain S, Wen Quan Lian D, Hong Pheng Loh A, Tan AM, et al. Primary adrenal angiomatoid fibrous histiocytoma with novel EWSR1-ATF1 gene fusion exon-exon breakpoint. Pediatr Dev Pathol. 2019;22(5):472–4.
4. Mangham DC, Williams A, Lalam RK, Brundler M-A, Leahy MG, Cool WP. Angiomatoid fibrous histiocytoma of bone: a calcifying sclerosing variant mimicking osteosarcoma. Am J Surg Pathol. 2010;34(2):279–85.
5. Bouma W, Koning KJ, Suurmeijer AJH, Slebos DJ, Mariani MA, Klinkenberg TJ. Hybrid bronchoscopic and surgical resection of endotracheal angiomatoid fibrous histiocytoma. J Cardiothorac Surg. 2019;14(1):48.
6. Gui H, Sussman RT, Jian B, Brooks JS, Zhang PJL. Primary pulmonary myxoid sarcoma and myxoid angiomatoid fibrous histiocytoma: a unifying continuum with shared and distinct features. Am J Surg Pathol. 2020;44(11):1535–40.
7. Kao Y-C, Lan J, Tai H-C, Li C-F, Liu K-W, Tsai J-W, et al. Angiomatoid fibrous histiocytoma: clinicopathological and molecular characterisation with emphasis on variant histomorphology. J Clin Pathol. 2014;67(3):210–5.
8. Moura RD, Wang X, Lonzo ML, Erickson-Johnson MR, García JJ, Oliveira AM. Reticular angiomatoid "malignant" fibrous histiocytoma–a case report with cytogenetics and molecular genetic analyses. Hum Pathol. 2011;42(9):1359–63.
9. Rekhi B, Adamane S, Ghodke K, Desai S, Jambhekar NA. Angiomatoid fibrous histiocytoma: clinicopathological spectrum of five cases, including EWSR1-CREB1 positive result in a single case. Indian J Pathol Microbiol. 2016;59(2):148–52.
10. Ren L, Guo S-P, Zhou X-G, Chan JKC. Angiomatoid fibrous histiocytoma: first report of primary pulmonary origin. Am J Surg Pathol. 2009;33(10):1570–4.
11. Schaefer I-M, Fletcher CDM. Myxoid variant of so-called angiomatoid "malignant fibrous histiocytoma": clinicopathologic characterization in a series of 21 cases. Am J Surg Pathol. 2014;38(6):816–23.
12. Thway K, Nicholson AG, Wallace WA, Al-Nafussi A, Pilling J, Fisher C. Endobronchial pulmonary angiomatoid fibrous histiocytoma: two cases with EWSR1-CREB1 and EWSR1-ATF1 fusions. Am J Surg Pathol. 2012;36(6):883–8.
13. Antonescu CR, Dal Cin P, Nafa K, Teot LA, Surti U, Fletcher CD, et al. EWSR1-CREB1 is the predominant gene fusion

in angiomatoid fibrous histiocytoma. Genes Chromosomes Cancer. 2007;46(12):1051–60.
14. Noujaim J, Jones RL, Swansbury J, Gonzalez D, Benson C, Judson I, et al. The spectrum of EWSR1-rearranged neoplasms at a tertiary sarcoma centre; assessing 772 tumour specimens and the value of current ancillary molecular diagnostic modalities. Br J Cancer. 2017;116(5):669–78.
15. Rossi S, Szuhai K, Ijszenga M, Tanke HJ, Zanatta L, Sciot R, et al. EWSR1-CREB1 and EWSR1-ATF1 fusion genes in angiomatoid fibrous histiocytoma. Clin Cancer. 2007;13(24):7322–8.
16. Thway K, Gonzalez D, Wren D, Dainton M, Swansbury J, Fisher C. Angiomatoid fibrous histiocytoma: comparison of fluorescence in situ hybridization and reverse transcription polymerase chain reaction as adjunct diagnostic modalities. Ann Diagn Pathol. 2015;19(3):137–42.
17. Hallor KH, Micci F, Meis-Kindblom JM, Kindblom L-G, Bacchini P, Mandahl N, et al. Fusion genes in angiomatoid fibrous histiocytoma. Cancer Lett. 2007;251(1):158–63.
18. Yoshida A, Wakai S, Ryo E, Miyata K, Miyazawa M, Yoshida K-I, et al. Expanding the phenotypic spectrum of mesenchymal tumors harboring the EWSR1-CREM fusion. Am J Surg Pathol. 2019;43(12):1622–30.
19. Thway K, Fisher C. Tumors with EWSR1-CREB1 and EWSR1-ATF1 fusions: the current status. Am J Surg Pathol. 2012;36(7):e1–11.
20. Alshareef MA, Almadidy Z, Baker T, Perry A, Welsh CT, Vandergrift WA. Intracranial angiomatoid fibrous histiocytoma: case report and literature review. World Neurosurg. 2016;96:403–9.
21. Bale TA, Oviedo A, Kozakewich H, Giannini C, Davineni PK, Ligon K, et al. Intracranial myxoid mesenchymal tumors with EWSR1-CREB family gene fusions: myxoid variant of angiomatoid fibrous histiocytoma or novel entity? Brain Pathol Zurich Switz. 2018;28(2):183–91.
22. Ballester LY, Meis JM, Lazar AJ, Prabhu SS, Hoang KB, Leeds NE, et al. Intracranial myxoid mesenchymal tumor with EWSR1-ATF1 fusion. J Neuropathol Exp Neurol. 2020;79(3):347–51.
23. Bin Abdulqader S, Altuhaini K, Tallab R, AlTurkistani A, Alhussinan M, Alghamdi S, et al. Primary intracranial angiomatoid fibrous histiocytoma: two case reports and literature review. World Neurosurg. 2020;143:398–404.
24. Choy B, Pytel P. Primary intracranial myoepithelial neoplasm: a potential mimic of meningioma. Int J Surg Pathol. 2016;24(3):243–7.
25. Domingo RA, Vivas-Buitrago T, Jentoft M, Quinones-Hinojosa A. Intracranial myxoid mesenchymal tumor/myxoid subtype angiomatous fibrous histiocytoma: diagnostic and prognostic challenges. Neurosurgery. 2020;88(1):E114–22.
26. Dunham C, Hussong J, Seiff M, Pfeifer J, Perry A. Primary intracerebral angiomatoid fibrous histiocytoma: report of a case with a t(12;22)(q13;q12) causing type 1 fusion of the EWS and ATF-1 genes. Am J Surg Pathol. 2008;32(3):478–84.
27. Ghanbari N, Lam A, Wycoco V, Lee G. Intracranial myxoid variant of angiomatoid fibrous histiocytoma: a case report and literature review. Cureus. 2019;11(3):e4261.
28. Gilbert AR, Yan L, McDougall CM. Broadening the age of incidence of intracranial angiomatoid fibrous histiocytoma with EWSR1-CREM fusion: a case report. J Neuropathol Exp Neurol. 2020;79(11):1244–6.
29. Hansen JM, Larsen VA, Scheie D, Perry A, Skjøth-Rasmussen J. Primary intracranial angiomatoid fibrous histiocytoma presenting with anaemia and migraine-like headaches and aura as early clinical features. Cephalalgia. 2015;35(14):1334–6.
30. Kao Y-C, Sung Y-S, Zhang L, Chen C-L, Vaiyapuri S, Rosenblum MK, et al. EWSR1 fusions With CREB family transcription factors define a novel myxoid mesenchymal tumor with predilection for intracranial location. Am J Surg Pathol. 2017;41(4):482–90.
31. Komatsu M, Yoshida A, Tanaka K, Matsuo K, Sasayama T, Kojita Y, et al. Intracranial myxoid mesenchymal tumor with EWSR1-CREB1 gene fusion: a case report and literature review. Brain Tumor Pathol. 2020;37(2):76–80.
32. Konstantinidis A, Cheesman E, O'Sullivan J, Pavaine J, Avula S, Pizer B, et al. Intracranial angiomatoid fibrous histiocytoma with EWSR1-CREB family fusions: a report of 2 pediatric cases. World Neurosurg. 2019;126:113–9.
33. Libbrecht S, Van Der Meulen J, Mondelaers V, Baert E, Vande Walle C, Van Dorpe J, et al. Intracranial myxoid mesenchymal tumor with EWSR1-CREB1 fusion. Pathol Res Pract. 2020;216(12):153239.
34. Lopez-Nunez O, Cafferata B, Santi M, Ranganathan S, Pearce TM, Kulich SM, et al. The spectrum of rare central nervous system (CNS) tumors with EWSR1-non-ETS fusions: experience from three pediatric institutions with review of the literature. Brain Pathol. 2021;31:70–83.
35. Ochalski PG, Edinger JT, Horowitz MB, Stetler WR, Murdoch GH, Kassam AB, et al. Intracranial angiomatoid fibrous histiocytoma presenting as recurrent multifocal intraparenchymal hemorrhage. J Neurosurg. 2010;112(5):978–82.
36. Sciot R, Jacobs S, Calenbergh FV, Demaerel P, Wozniak A, Debiec-Rychter M. Primary myxoid mesenchymal tumour with intracranial location: report of a case with a EWSR1-ATF1 fusion. Histopathology. 2018;72(5):880–3.
37. Sion AE, Tahir RA, Mukherjee A, Rock JP. Cranial angiomatoid fibrous histiocytoma: a case report and review of literature. Surg Neurol Int. 2020;11:295.
38. Sloan EA, Chiang J, Villanueva-Meyer JE, Alexandrescu S, Eschbacher JM, Wang W, et al. Intracranial mesenchymal tumor with FET-CREB fusion - a unifying diagnosis for the spectrum of intracranial myxoid mesenchymal tumors and angiomatoid fibrous histiocytoma-like neoplasms. Brain Pathol. 2021;31(4):e12918.
39. Valente Aguiar P, Pinheiro J, Lima J, Vaz R, Linhares P. Myxoid mesenchymal intraventricular brain tumour with EWSR1–CREB1 gene fusion in an adult woman. Virchows Archiv. 2021;478(5):1019–24. https://doi.org/10.1007/s00428-020-02885-7.
40. Ward B, Wang CP, Macaulay RJB, Liu JKC. Adult intracranial myxoid mesenchymal tumor with EWSR1-ATF1 gene fusion. World Neurosurg. 2020;143:91–6.
41. White MD, McDowell MM, Pearce TM, Bukowinski AJ, Greene S. Intracranial myxoid mesenchymal tumor with rare EWSR1-CREM translocation. Pediatr Neurosurg. 2019;54(5):347–53.
42. Gareton A, Pierron G, Mokhtari K, Tran S, Tauziède-Espariat A, Pallud J, et al. ESWR1-CREM fusion in an intracranial myxoid angiomatoid fibrous histiocytoma-like tumor: a case report and literature review. J Neuropathol Exp Neurol. 2018;77(7):537–41.
43. Koelsche C, Schrimpf D, Stichel D, Sill M, Sahm F, Reuss DE, et al. Sarcoma classification by DNA methylation profiling. Nat Commun. 2021;12(1):498.
44. Hovestadt V, Jones DTW, Picelli S, Wang W, Kool M, Northcott PA, et al. Decoding the regulatory landscape of medulloblastoma using DNA methylation sequencing. Nature. 2014;510(7506):537–41.
45. Kida S, Yamashima T, Kubota T, Ito H, Yamamoto S. A light and electron microscopic and immunohistochemical study of human arachnoid villi. J Neurosurg. 1988;69(3):429–35.
46. Satomi T, Hasegawa O, Abukawa H, Kohno M, Enomoto A, Chikazu D, et al. Exceptionally large solitary fibrous tumor arising from the cheek: an immunohistochemical and ultrastructural study with a review of the literature. Med Mol Morphol. 2014;47(2):108–16.
47. Rodríguez-Gil Y, González MAM, Carcavilla CB, Santamaría JS. Lines of cell differentiation in solitary fibrous tumor: an ultrastructural and immunohistochemical study of 10 cases. Ultrastruct Pathol. 2009;33(6):274–85.

48. Hasegawa T, Seki K, Ono K, Hirohashi S. Angiomatoid (malignant) fibrous histiocytoma: a peculiar low-grade tumor showing immunophenotypic heterogeneity and ultrastructural variations. Pathol Int. 2000;50(9):731–8.
49. Vizcaino MA, Giannini C, Chang HT, Kipp BR, Fritchie K, Vaubel R. Intracranial angiomatoid fibrous histiocytoma with rhabdoid features: a mimic of rhabdoid meningioma. Brain Tumor Pathol. 2021;38(2):138–44.
50. Go K, Lee K, Heo W, Lee YS, Park Y-S, Kim SK, et al. Cystic meningiomas: correlation between radiologic and histopathologic features. Brain Tumor Res Treat. 2018;6(1):13–21.
51. Surov A, Gottschling S, Mawrin C, Prell J, Spielmann RP, Wienke A, et al. Diffusion-weighted imaging in meningioma: prediction of tumor grade and association with histopathological parameters. Transl Oncol. 2015;8(6):517–23.
52. Maeda M, Matsumine A, Kato H, Kusuzaki K, Maier SE, Uchida A, et al. Soft-tissue tumors evaluated by line-scan diffusion-weighted imaging: influence of myxoid matrix on the apparent diffusion coefficient. J Magn Reson Imaging. 2007;25(6):1199–204.
53. Surov A, Meyer HJ, Wienke A. Correlation between apparent diffusion coefficient (ADC) and cellularity is different in several tumors: a meta-analysis. Oncotarget. 2017;8(35):59492–9.
54. Johnson MD, Hussain A. Imaging and clinicopathologic features of myxoid meningiomas. Clin Neuropathol. 2019;38(5):238–44.
55. Salle H, Durand K, Gantois C, Labrousse F, Duchesne M. Myxoid meningioma: first report of a rare metaplastic meningioma variant in the pineal region. J Neuropathol Exp Neurol. 2021;80(1):96–100.
56. Menke JR, Raleigh DR, Gown AM, Thomas S, Perry A, Tihan T. Somatostatin receptor 2a is a more sensitive diagnostic marker of meningioma than epithelial membrane antigen. Acta Neuropathol (Berl). 2015;130(3):441–3.
57. Bauer A, Jackson B, Marner E, Gilbertson-Dahdal D. Angiomatoid fibrous histiocytoma: a case report and review of the literature. J Radiol Case Rep. 2012;6(11):8–15.
58. Akiyama M, Yamaoka M, Mikami-Terao Y, Yokoi K, Inoue T, Hiramatsu T, et al. Paraneoplastic syndrome of angiomatoid fibrous histiocytoma may be caused by EWSR1-CREB1 fusion-induced excessive interleukin-6 production. J Pediatr Hematol Oncol. 2015;37(7):554–9.
59. Ghigna M-R, Hamdi S, Petitpretz P, Rohnean A, Florea V, Mussot S, et al. Angiomatoid fibrous histiocytoma of the pulmonary artery: a multidisciplinary discussion. Histopathology. 2014;65(2):278–82.
60. Hallor KH, Mertens F, Jin Y, Meis-Kindblom JM, Kindblom L-G, Behrendtz M, et al. Fusion of the EWSR1 and ATF1 genes without expression of the MITF-M transcript in angiomatoid fibrous histiocytoma. Genes Chromosomes Cancer. 2005;44(1):97–102.
61. Jelti L, Alorini M, Boivin C, Courville P, Balguerie X, Bonmarchand A, et al. Angiomatoid fibrous histiocytoma of the radial pulse groove. Ann Dermatol Venereol. 2018;145(12):756–60.
62. Potter SL, Quintanilla NM, Johnston DK, Naik-Mathuria B, Venkatramani R. Therapeutic response of metastatic angiomatoid fibrous histiocytoma carrying EWSR1-CREB1 fusion to the interleukin-6 receptor antibody tocilizumab. Pediatr Blood Cancer. 2018;65(10):e27291.
63. Sparreboom E, Wetzels C, Verdijk M, Mulder S, Blokx W. Subcutaneous angiomatoid fibrous histiocytoma mimicking metastatic melanoma. Case Rep Pathol. 2012;2012:291623.
64. Thway K, Strauss DC, Wren D, Fisher C. "Pure" spindle cell variant of angiomatoid fibrous histiocytoma, lacking classic histologic features. Pathol Res Pract. 2016;212(11):1081–4.
65. Antonescu CR, Tschernyavsky SJ, Woodruff JM, Jungbluth AA, Brennan MF, Ladanyi M. Molecular diagnosis of clear cell sarcoma: detection of EWS-ATF1 and MITF-M transcripts and histopathological and ultrastructural analysis of 12 cases. J Mol Diagn JMD. 2002;4(1):44–52.
66. Chang B, Yu L, Guo W-W, Sheng W-Q, Wang L, Lao I, et al. Malignant gastrointestinal neuroectodermal tumor: clinicopathologic, immunohistochemical, and molecular analysis of 19 cases. Am J Surg Pathol. 2020;44(4):456–66.
67. Li R, Cao J, Chen L, Cui F, Chen S, Feng Z, et al. Malignant gastrointestinal neuroectodermal tumors: clinicopathological and prognostic features of 96 patients. OncoTargets Ther. 2020;13:9731–40.

SUPPORTING INFORMATION

Additional Supporting Information may be found online in the Supporting Information section.

FIGURE S1 Expression data analysis by unsupervised clustering using Inter Quantile Range (IQR) and Spearman's correlation. The comparison of solitary fibrous tumors (n = 26) (red – cluster A), meningiomas (n = 25) (green – cluster B) or tumors harboring *EWSR1 :CREB* family genes fusions (cluster C) showed a clustering according to the tumor type, independently of the organ. The last subgroup is composed of clear cell sarcomas (n = 9) (blue), angiomatoid fibrous histiocytomas (n = 6) (dark) including four cases of the CNS (orange)

FIGURE S2 Ultrastructural analyses. (A) Presence of *zonula occludens*. (B) Presence of desmosomes (white arrow), *zonula adherens* (black arrow), and collagen (asterisk) in tumor cells

Table S1 Histopathological and molecular findings of cases of our series

How to cite this article: Tauziède-Espariat A, Sievers P, Larousserie F, Benzakoun J, Guillemot D, Pierron G, et al; the RENOCLIP-LOC. An integrative histopathological and epigenetic characterization of primary intracranial mesenchymal tumors, FET:CREB-fused broadening the spectrum of tumor entities in comparison with their soft tissue counterparts. Brain Pathology. 2022;32:e13010. https://doi.org/10.1111/bpa.13010